

Integration of GOCI and AHI Yonsei Aerosol Optical Depth Products During the 2016 KORUS-AQ and 2018 EMeRGe Campaigns

Hyunkwang Lim¹, Sujung Go^{1,a}, Jhoon Kim^{1,2}, Myungje Choi^{1,a}, Seoyoung Lee¹, Chang-Keun Song³, Yasuko Kasai⁴

¹Department of Atmospheric Sciences, Yonsei University, Seoul 03722, Republic of Korea

²Particulate Matter Research Institute, Samsung Advanced Institute of Technology, Suwon 16678, Republic of Korea

³School of Urban and Environmental Engineering, Ulsan National Institute of Science and Technology, Ulsan 44919, Republic of Korea

⁴National Institute of Information and Communications Technology, Tokyo 184-8759, Japan

Correspondence to: Jhoon Kim (jkim2@yonsei.ac.kr)

^aCurrent address: Joint Center for Earth Systems Technology, University of Maryland, Baltimore County, Baltimore, MD 21250, USA, and NASA Goddard Space Flight Center, Greenbelt, MD 20771, USA.

Abstract. The Yonsei Aerosol Retrieval (YAER) algorithm for the Geostationary Ocean Color Imager (GOCI) retrieves aerosol optical properties only over dark surfaces, so it is important to mask pixels with bright surfaces. The Advanced Himawari Imager (AHI) is equipped with three shortwave-infrared and nine infrared channels, which is advantageous for bright-pixel masking. In addition, multiple visible and near-infrared channels provide a great advantage in aerosol property retrieval from the AHI and GOCI. By applying the YAER algorithm to 10 minute AHI or 1 hour GOCI data at $6 \text{ km} \times 6 \text{ km}$ resolution, diurnal variations and aerosol transport can be observed, which has not previously been possible from low-earth-orbit satellites. This study attempted to estimate the optimal aerosol optical depth (AOD) for East Asia by data fusion, taking into account satellite retrieval uncertainty. The data fusion involved two steps: (1) analysis of error characteristics of each retrieved result with respect to the ground-based Aerosol Robotic Network (AERONET), and bias correction based on normalized difference vegetation indexes; and (2) compilation of the fused product using ensemble-mean and maximum-likelihood estimation methods (MLE). Fused results show a better statistics in terms of fraction within the expected error, correlation coefficient, root-mean-square error, median bias error than the retrieved result for each product. If the root mean square error and mean AOD bias values used for MLE fusion are correct, the MLE fused products show better accuracy, but the ensemble-mean products can still be used as useful as MLE.

1. Introduction

Aerosols are generated by human activities and natural processes on local to global scales, and have a lifetime of several to tens of days. Aerosols affect Earth's radiative energy balance by scattering and absorption (e.g. Cho et al., 2003). High aerosol loadings are persistent in

41 Northeast Asia, including diverse aerosol types from various sources. Interactions among
42 aerosols, clouds, and radiation in the atmosphere cause significant uncertainties in climate-
43 model calculations (IPCC, 2013). Datasets produced by satellites have been widely used to
44 reduce such uncertainties (Saide et al., 2014; Pang et al., 2018), but the systems must be
45 accurately calibrated, verified, and consistent. Satellite data have been used extensively to
46 retrieve aerosol optical properties (AOPs) over broad areas, with several algorithms having
47 been developed. Satellites in low earth orbit (LEO), including Sun-synchronous orbit (SSO),
48 cover the entire Earth over one to several days, depending on instrument and orbit
49 characteristics. Most aerosol retrieval algorithms have been developed for LEO satellites
50 (Kim et al., 2007; Lyapustin et al., 2011a, b; Lee et al., 2012; Fukuda et al., 2013; Hsu et al.,
51 2013; Levy et al., 2013; Garay et al., 2017, 2020). LEO instruments currently onboard
52 satellites include the Moderate Resolution Imaging Spectrometer (MODIS), Visible Infrared
53 Imaging Radiometer Suite (VIIRS), Multi-angle Imaging SpectroRadiometer (MISR), and
54 Cloud and Aerosol Imager (CAI) (Remer et al., 2005; Lyapustin et al., 2011a, b, 2018;
55 Fukuda et al., 2013; Hsu et al., 2013; Levy et al., 2013; Garay et al., 2017, 2020; Jackson et
56 al., 2013; Lee et al., 2017).

57 Representative algorithms developed for MODIS data include the Dark-Target (DT; Remer
58 et al., 2005; Levy et al., 2013), Deep Blue (DB; Hsu et al., 2013; Sayer et al., 2014), and
59 Multi-Angle Implementation of Atmospheric Correction (MAIAC; Lyapustin et al., 2011a, b)
60 systems, which are also applied for the succeeding VIIRS (Sayer et al., 2018). In the DT
61 algorithm, the 2.1 μm channel is used to estimate land-surface reflectance in the visible (VIS)
62 region using empirical equations based on the normalized difference vegetation index
63 (NDVI). The DT algorithm has improved surface-reflectance modelling through
64 consideration of the fractional area of urbanization (Gupta et al., 2016). Ocean-surface
65 reflectance is estimated using the Cox and Munk method (Cox and Munk, 1954), and AOPs
66 over land and ocean are provided at spatial resolutions of 10 km \times 10 km and 3 km \times 3 km
67 (Remer et al., 2013), respectively. The DB algorithm has an advantage over the DT algorithm
68 in allowing aerosol data retrieval over bright surfaces. By using a shorter-wavelength channel,
69 accuracy is improved over bright surfaces such as urban and desert areas, where surface
70 reflectance was previously estimated by the minimum reflectance method (MRM; Herman
71 and Celarier 1997; Koelemeijer et al., 2003; Hsu et al., 2004). Furthermore, with the
72 improvement to Collection 6.1, land-surface reflectance can be estimated similarly to the DT
73 method, over densely vegetated regions (Sayer et al., 2019). In the case of VIIRS DB, aerosol
74 retrieval over the ocean is also applied by the Satellite Ocean Aerosol Retrieval (SOAR)
75 algorithm (Sayer et al., 2018). In the MODIS MAIAC system, surface reflectance is
76 estimated by considering various images based on time-series analysis, with multi-angle
77 observations, based on up to 16 day data, and by applying the bidirectional reflectance
78 distribution function (BRDF). Ocean-surface reflectance is determined using a Cox and
79 Munk BRDF model similar to DT and VIIRS DB (Lyapustin et al., 2011a, b, 2018). The
80 MISR observes Earth at nine different angles, providing a high degree of freedom for signals;
81 consequently, retrievals yield estimates of aerosol type and shape. As with the MAIAC,
82 multiple observations are used, with the estimation of land-surface reflectance involving
83 bidirectional reflectance factors (BRF). Zhang et al. (2016) developed an aerosol retrieval
84 algorithm that allows aerosol data retrieval over bright land surfaces using surface-reflectance
85 ratios from the VIIRS.

86 Aerosol retrieval algorithms for geosynchronous Earth orbit (GEO) satellites have been
87 developed, including the Geostationary Operational Environmental Satellite (GOES) series in
88 the USA (Knapp et al., 2005), Meteosat series in Europe (Bernard et al., 2011), Himawari
89 series in Japan (Yoon et al., 2007; Kim et al., 2008; Lim et al., 2018; Kikuchi et al., 2018;

90 Yoshida et al., 2018; Gupta et al., 2019), and the Geostationary Korea Multi-Purpose Satellite
91 (GEO-KOMPSAT, GK) series in South Korea (Kim et al., 2014, 2016; Choi et al., 2016,
92 2018; Kim et al., 2020). However, previously launched geostationary meteorological
93 satellites had only a single, broadband VIS channel, with which it is difficult to retrieve
94 AOPs other than aerosol optical depth (AOD) (Wang et al., 2003; Knapp et al., 2005; Kim et
95 al., 2008, 2014, 2016; Bernard et al., 2011). However, the Geostationary Ocean Color Imager
96 (GOCI) onboard the GK-1 satellite, also known as the Communication, Ocean, and
97 Meteorological Satellite (COMS), has six VIS and two near-infrared (NIR) channels, which
98 is advantageous for retrieving AOPs (Lee et al., 2010; Choi et al., 2016, 2018; Kim et al.,
99 2017). Next-generation meteorological GEO satellite instruments, including the Advanced
100 Himawari Imager (AHI), Advanced Baseline Imager (ABI), and Advanced Meteorological
101 Imager (AMI), have three to four VIS and NIR channels, which enable aerosol property
102 retrieval with high accuracy (Lim et al., 2016, 2018; Kikuchi et al., 2018; Yoshida et al.,
103 2018; Gupta et al., 2019). Kikuchi et al. (2018) and Yoshida et al. (2018) performed aerosol
104 retrievals using the MRM and corrected reflectance using empirical equations. Gupta et al.
105 (2019) extended the MODIS DT algorithm to GEO satellites and estimated visible surface
106 reflectance using SWIR reflectance. Lim et al. (2018) retrieved the AOPs using both MRM
107 and estimated surface reflectance from short-wave IR (SWIR) data (ESR), and presented the
108 two merged products: an L2-AOD merged product, and a reprocessed AOD produced by
109 merging MRM and ESR surface reflectances. The MRM gives better accuracy over brighter
110 surfaces such as urban areas, while the ESR method gives better accuracy over areas of dense
111 vegetation (Lim et al., 2018). However, there is a critical surface reflectance at which aerosol
112 signals disappear, depending on the single-scattering albedo (Kim et al., 2016). Over the
113 ocean, both the MRM and ESR methods give high accuracy, but ESR results are robust with
114 the Cox and Munk model.

115 The MRM requires more computational time than the ESR method to estimate surface
116 reflectance, as it requires data for the past 30 days, and LER needs to be calculated using a
117 radiative transfer model. The ESR method estimates surface reflectance from the observed
118 TOA reflectance at 1.6 μm wavelength using empirical equations including the NDVI. The
119 advantage of MRM is that stable surface reflectance values can be obtained regardless of
120 surface type. However, due to the influence of background aerosol optical depth (BAOD),
121 surface reflectance tends to be overestimated, with satellite-derived AOD data thus being
122 underestimated (Kim et al., 2014). On the other hand, the ESR method uses TOA reflectance
123 at 1.6 μm wavelength to detect surface signals, which is less sensitive to fine particles and
124 BAOD. However, when aerosols such as yellow dust with coarse particles are transported
125 from the Taklamakan and Gobi deserts, the BAOD effect also applies to the ESR method.
126 The ESR method is also more likely to be affected by snow surfaces than the MRM, as snow
127 reduces reflectivity around the 1.6 μm wavelength (Negi and Kokhanovsky, 2011). The ESR
128 method also has the disadvantage of giving noisy results over bright surfaces such as desert.
129 However, its fast surface-reflectance estimation enables near-real-time retrieval based on the
130 AHI YAER algorithm.

131

132 Algorithms developed to date for LEO and GEO satellites have both advantages and
133 disadvantages, depending on algorithm characteristics. Therefore, the MODIS team provides
134 combined DT and DB AOD products (Levy et al., 2013; Sayer et al., 2014). In addition,
135 several studies of the fusion of L2 products have been conducted (Levy et al., 2013; Sayer et
136 al., 2014; Wei et al., 2019), with Bilal et al. (2017) obtaining reliable results from merged DT
137 and DB products, as indicated by the NDVI in East Asia, and also robust products by simply
138 averaging DT and DB without consideration of the NDVI.

139 AOP data fusion in East Asia may also be achieved using aerosol products of AMI, GOCI-2,
140 and the geostationary environment monitoring spectrometer (GEMS) onboard the GK-2A and
141 2B satellites launched by South Korea in 2018 and 2020, respectively, with accuracy over
142 bright surfaces being improved by the GEMS aerosol product. It is also possible to obtain
143 accurate AOPs such as single-scattering albedo and fine-mode fraction, and aerosol loading
144 height, which have been difficult to obtain by fusion of L2 data and/or surface reflectance
145 data. If the trace-gas dataset retrieved from GEMS is used, it is possible to improve the
146 aerosol type, with the retrieval of high-quality AOD data (Go et al., 2020).

147 Several studies have considered AOD data fusion, for which methods can be broadly
148 classified into two types. First, the fusion of more than one AOD product may involve
149 optimal interpolation (Xue et al., 2012), linear or second-order polynomial functions (Mélin
150 et al., 2007), arithmetic or weighted means (Gupta et al., 2008), or maximum-likelihood
151 estimates (MLE) (Nirala, 2008; Xu et al., 2015; Xie et al., 2018). Second, in the absence of
152 satellite-derived AOD products for the day of fusion, the geostatistical fusion method,
153 universal kriging method (Chatterjee et al., 2010; Li et al., 2014), geostatistical inverse
154 modelling (Wang et al., 2013), or spatial statistical data fusion (Nguyen et al., 2012) may be
155 applied. These have the advantage that AOD can be estimated by integrating the spatial
156 autocorrelation of AOD data even for pixels missing from the AOD products, although there
157 is a disadvantage in not considering temporal correlations. The Bayesian maximum entropy
158 (BME) method, taking into account temporal autocorrelation, has also been developed (Tang
159 et al., 2016). BME methodology can estimate gap-filling pixels that are difficult to retrieve
160 due to clouds, but with somewhat reduced accuracy. Gap filled AOD using the BME method,
161 and satellite-derived AOD discontinuity arises from insufficient temporal sampling being
162 available with the use of LEO satellites, resulting in a low fusion synergy. Previous studies
163 mentioned above include data fusion based on Kriging, reproduction of spectral AOD, and
164 BME method. Most of them focus on gap filling and rebuild AOD in areas not observed by
165 MISR, MODIS, and SeaWiFS, and so on (Wang et al., 2013; Tang et al., 2016). However in
166 this study, we focused on optimized AOD products with improved accuracy at the retrieved
167 pixels by ensemble-mean and MLE fusion. We compared these two products, one very
168 simple one and the other with more elaborated processes. As previous AOD fusion studies
169 improved the retrieved results mainly based on MLE or NDVI-based fusion studies (Bilal et
170 al., 2017; Levy et al., 2013; Wei et al., 2019; Go et al., 2020), we tried to further improve
171 them with efficient approach to save computation time considering the nature of satellite data
172 file size and user's near-real-time demand for data assimilation.

173 In this study, the GEO satellite dataset was used to resolve the temporal sampling issue for
174 data fusion, while maintaining the spatio-temporal resolution retrieved from GEO satellites.
175 We also attempted to estimate fused AOD products at 550nm with higher accuracy in East
176 Asia. The ensemble-mean and MLE methods were applied. Section 2 describes the two
177 algorithms used in this study for AHI and GOCI. Section 3 mentions methods of fusion and
178 systematic bias correction, and section 4 performs validation of the fused products with the
179 Aerosol Robotic Network (AERONET) instruments during two field campaigns: the Korea–
180 United States Air Quality Study (KORUS-AQ) and the Effect of Megacities on the Transport
181 and Transformation of Pollutants on Regional and Global Scales Study (EMeRGe).

182 **2. Descriptions of AHI, GOCI, the YAER algorithm**

183 **2.1 AHI aerosol algorithm**

184 The Himawari-8 and -9 satellites were launched by the Japanese Meteorological Agency
185 (JMA) on 7 October 2014 and 2 November 2016, respectively. The AHI onboard these
186 satellites has 16 channels covering wavelengths of 0.47–13.3 μm and performs full-disk and
187 Japan-area observations every 10 and 2.5 min, respectively, from GEO at 140.7° E longitude
188 (Bessho et al., 2016). Visible and NIR observations are also performed at high spatial
189 resolutions of 0.5–1.0 km, with SWIR to IR at 2 km, which have advantages in aerosol
190 property retrieval and cloud masking.

191 Lim et al. (2018) developed the AHI Yonsei aerosol retrieval (YAER) algorithm and
192 provided two retrieval results with 6 km \times 6 km resolution based on MRM and ESR using
193 SWIR data. Aerosol property retrieval using VIS channels requires accurate surface
194 reflectance, for which MRM and ESR are useful, with the main difference between the two
195 lying in the surface-reflectance estimation method.

196 The MRM applies the minimum-reflectance technique over both land and ocean (Lim et al.,
197 2018), with surface reflectance being estimated by finding the minimum reflectance in each
198 pixel over the past 30 day window, giving the Lambertian equivalent reflectance (LER; Kim
199 et al., 2016; Lim et al., 2018). This method takes the bidirectional characteristics of surface
200 reflectance into consideration by obtaining surface reflectance at each observation time over
201 the 30-day search window. However, the method assumes that there is more than one clear
202 day during the search window and that surface reflectance does not change; otherwise, it is
203 affected by clouds and/or the BAOD (Kim et al., 2014; Kim et al., 2021).

204 According to the ESR method, land-surface reflectance in the VIS region is constructed
205 from the Top of Atmosphere (TOA) reflectance at 1.6 μm wavelength, based on the NDVI
206 for SWIR and the fraction of urbanization and cropland (Levy et al 2013; Gupta et al., 2016;
207 Zhong et al., 2016; Lim et al., 2018). Ocean-surface reflectance is estimated from the Cox
208 and Munk BRDF model (Cox and Munk, 1954). Chlorophyll-a concentrations are considered
209 in addition to Chlorophyll-a concentration data
210 (<https://www.eorc.jaxa.jp/ptree/userguide.html>) from Japan Aerospace Exploration Agency
211 (JAXA) (Murakami et al., 2016) and interpolated for the 10-min AHI intervals. For
212 unretreived pixels, the less contaminated chlorophyll-a concentration value of 0.02 mg m^{-3} is
213 used. Details of the methodology can be found in Lim et al. (2018).

214 **2.2 GOCI aerosol algorithm**

215 GOCI is an ocean color imager in GEO launched onboard COMS in 2010 and observes the
216 East Asia region at an hourly interval with 500 m \times 500 m resolution (Choi et al., 2012). It has
217 eight bands in the VIS and NIR regions, which is advantageous for aerosol retrieval. Two
218 versions of GOCI Yonsei aerosol algorithms have been developed, referred to as V1 and V2
219 (Lee et al., 2010; Choi et al., 2016, 2018). In the case of V1, surface reflectance is estimated
220 by the MRM using LER for the past 30 days over land, and the Cox and Munk BRDF model
221 over oceans. In V2, ocean-surface reflectance is estimated by the same method, but land-
222 surface reflectance is improved by using an accumulated long-term database. To minimize
223 the impact of BAOD (the weakness of the MRM), a monthly surface-reflectance database
224 was constructed using all of the LERs over the past five years, but it cannot reflect
225 unexpected changes in surface conditions. However, a well-established climatological
226 database allows aerosol property retrieval in near-real-time with reasonable accuracy.

227

228 3. Data fusion methods

229 Satellite-derived AODs have different error characteristics depending on NDVI, scattering
230 angle, and so on (Choi et al., 2016, 2018; Lim et al., 2018). Over oceans, ESR AODs are
231 more accurate than MRM AODs. However, the accuracy of GOCI AODs was dependent on
232 the NDVI values, which represent surface condition in terms of vegetation. V1 has a negative
233 bias and V2 has a mostly a positive bias (Choi et al., 2018). In this study, we developed
234 optimal AOD products at 550 nm in East Asia by fusing four individual retrievals, i.e. two
235 AHI aerosol products from the MRM and ESR methods, and two GOCI products from V1
236 and V2.

237 3.1 Spatio-temporal matching

238 The AHI and GOCI have different spatial pixel locations and temporal resolutions, so it is
239 necessary to match their spatio-temporal resolutions before data fusion. GOCI and AHI
240 AODs have the same spatial resolution of $6 \text{ km} \times 6 \text{ km}$, but the two satellites are located at
241 128.2° E and 140.7° E , respectively, at the equator. Spatial pixel matching is therefore
242 required. However, satellite-derived AOD represents total-column extinction, so AOD
243 retrieved by the two sensors is not significantly affected by satellite position. To merge the
244 different satellite spatial pixel coverages, the GOCI pixel was re-gridded to match AHI pixels
245 for full-disk observation, with up to 4 GOCI AOD pixels being used with average values
246 considered representative of pixel values. If more than half of the AHI AOD pixels did not
247 exist out of the maximum 6 AHI data per hour, it is regarded as cloud contaminated pixels
248 and an additional cloud removal process is performed. This process applies to both the MRM
249 and ESR method, to remove the AHI's additional cloud-contaminated pixels in products of
250 both GOCI V1 and V2, which have a disadvantage in cloud masking due to their lack of IR
251 channels. When three or more pixels were available for generating AHI data at 1 hour
252 intervals, hourly AOD values were estimated as the medians of pixel values.

253 3.2 Ensemble-mean method

254 Here, AMR represents AHI MRM AOD, AES represents AHI ESR AOD, GV1 represents
255 GOCI V1 AOD, and GV2 represents GOCI V2 AOD. We performed data fusion using AMR,
256 AES, GV1, and GV2 data within 1 hour intervals for which additional-cloud masking was
257 performed. The ensemble-mean is the mean of the ensemble member over a specific time.
258 The ensemble members are AMR, AES, GV1, and GV2 based on two satellite instruments
259 and two different surface-estimation methodologies. Table 1 provides the satellite-derived
260 AOD used for ensemble-mean and MLE fusion.

261 Fusion was performed only when a pixel of an ensemble member was used for all fusions.
262 Fusion 1 (F1) included the two AHI products of AMR and AES, and two GOCI products of
263 GV1 and GV2. Fusion 2 (F2) involved the calculation of the YAER algorithm by the fusion
264 of AES and GV2, both of which have the advantage of producing data in near-real-time.
265 Fusion 3 (F3) merged AMR and AES to estimate AOD over a wide area, and Fusion 4 (F4)
266 involved a comparison with F1 to determine how accuracy varied with decreasing number of
267 ensemble members, as summarized in Table 1.

268 3.3 MLE method

269 Similarly, FM1, FM2, and FM3 is the result of MLE fusion corresponding to F1, F2, and F3
270 as in ensemble mean, respectively (see Table 1).

271 The MLE method provides a means of weighting and averaging based on errors evaluated
 272 with AERONET ground-based measurements (Nirala, 2008; Xu et al., 2015; Xie et al., 2018).
 273 This method employs the following equations:

$$\tau_i^{MLE} = \sum_{k=1}^N \frac{R_{i,k}^{-2}}{\sum_{k=1}^N R_{i,k}^{-2}} \tau_{i,k} \quad (1)$$

$$R_{i,k} = \sqrt{\frac{\sum_{i=1}^M (s_{i,k} - g_i)^2}{M}} \quad (2)$$

274 where τ_i^{MLE} represents the fused AOD; $\tau_{i,k}$ represents the mean AOD at grid point i from the
 275 satellite-derived AOD product k , where k is the index for different satellite-derived AOD
 276 products for fusion; $R_{i,k}$ represents the root-mean-square error (RMSE) at grid point i for the
 277 satellite-derived AOD product k ; N is the number of all AOD data; g_i represents the mean of
 278 ground-based AOD at grid point i from the AERONET (collocated temporal mean); $s_{i,k}$
 279 represents the mean of satellite derived AOD products (k) at grid points of the AERONET
 280 (collocated spatial mean); and M is the number of pairs of $s_{i,k}$ and g_i .

281 For RMSE estimation, bias correction, validation, and error estimation (details in Sec.5),
 282 AERONET Version 3 Level 2.0 aerosol products were used for ground truth (Giles et al.,
 283 2019; Smirnov et al., 2000; Holben et al., 2001). RMSE and bias correction value for each
 284 satellite product (details in Sec.3.4) required for MLE fusion were calculated through
 285 comparison with AERONET from Apr. 2018 to Mar. 2019 excluding EMeRGe period. The
 286 number of AERONET sites used for validation and error estimation in this study, was 35
 287 during the KORUS-AQ campaign, and 22 during the EMeRGe campaign, for AHI and GOCI
 288 products.

289 Satellite observation can cover wide areas, but the ground observation instrument cannot
 290 cover all satellite observed areas. Therefore, a RMSE model was constructed for AOD, time,
 291 and NDVI through comparative validation with AERONET observation as shown in Figure 1.
 292 For MLE over wide areas without ground measurements, the calculated RMSE from AOD,
 293 time, and NDVI bins was applied for every satellite pixel. We excluded points that AOD
 294 differences with respect to AERONET data (dAOD) were > 2 standard deviations (SD) to
 295 remove outliers and to consider only the more stable RMSE values. According to Figure 1, if
 296 the AOD is less than 0.5, RMSE is about 0.1 with respect to all NDVI bins, but if the AOD is
 297 greater than 0.5, the overall RMSE value becomes large. All products excluding AES show
 298 large variations for high NDVI and high AOD bin as shown as the red square in Figure 1,
 299 especially for 02 UTC and 05 UTC of two GOCI products and 00 UTC in AMR product.
 300 This is because the two GOCI products and AMR are relatively less accurate for densely
 301 vegetated areas, along with sampling issues.

302 3.4 Bias correction

303 AOD follows a log-normal distribution (Sayer and Knobelspiesse, 2019), but dAOD for
 304 each satellite product follow a Gaussian distribution. The quantile–quantile (Q-Q) plot is a
 305 graphical statistical technique that compares two probability distributions with each other.
 306 The x-axis represents the quantile value of the directly calculated sample, and the y-axis
 307 represents the Z-score. Here, the Z-score is a dimensionless value that makes a statistically
 308 Gaussian distribution and shows where each sample is located on the standard deviation. That

309 is, when Z-score of 1 and 2 represent 1 SD and 2 SD, respectively. In addition, if the Q-Q
310 plot shows a linear shape, the sample is regarded as to follow a Gaussian distribution.

311 Figure 2 shows dAOD divided by SD analyzed for each satellite product, for the period
312 from April 2018 to March 2019, excluding the EMeRGe campaign, which shows a similar
313 pattern to the standard Gaussian distribution. However, if the theoretical quantile values are
314 greater than 0.5, then the sample quantile values are smaller than the standard Gaussian
315 values. Also, when the theoretical quantile is less than 0.5, the opposite results are shown.
316 Thus, the sample quantiles are more skewed at both sides than the theoretical quantile, but the
317 respective satellite product is assumed to follow the Gaussian distribution.

318 The bias center for each satellite product was calculated differently for time and NDVI bins
319 through Gaussian fitting in Figure 3 of the dAOD divided by SD (except for 2SD and higher),
320 and subtracted from respective product for correction. Data beyond 2 SD of dAOD were
321 excluded to prevent a change in bias trends due to AOD errors caused by cloud shadows and
322 cloud contamination. This process was performed before applying the MLE method, which
323 allows compensation for systematic bias that is difficult to obtain directly in MLE.
324

325 **3.5 Evaluation of aerosol products during two field campaigns**

326 The performance of the respective satellite product and fused products was analyzed in two
327 field campaigns: the KORUS-AQ of 1 May 2016 to 12 Jun 2016 ([https://www-
328 air.larc.nasa.gov/missions/korus-aq/](https://www-air.larc.nasa.gov/missions/korus-aq/)), and the EMeRGe of 12 Mar 2018 to 8 Apr 2018
329 (<https://www.halo.dlr.de/science/missions/emerge/emerge.html>). KORUS-AQ was an
330 international multi-organization mission to observe air quality across the Korean Peninsula
331 and surrounding waters, led by the US National Aeronautics and Space Administration
332 (NASA) and the Korean National Institute of Environmental Research (NIER) (Crawford et
333 al., 2021). EMeRGe aimed to investigate experimentally the patterns of atmospheric transport
334 and transformation of pollution plumes originating from Eurasia, tropical and subtropical
335 Asian megacities, and other major population centers. GEO satellite data played an important
336 role in these campaigns; e.g., data assimilation for chemical transport models and tracking
337 aerosol plumes (Saide et al., 2014, 2010; Pang et al., 2018).

338 In this study, we used satellite-derived GOCI and AHI AODs, with a spatial resolution of 6
339 km × 6 km, and temporal resolutions of 1 hour and 10 minutes, respectively. Spatio-temporal
340 correlation between satellite-derived AOD and AERONET AOD involved data averaged over
341 all satellite pixels within a 25 km radius of the AERONET site, and AERONET AOD
342 averaged over ±30 minutes from the satellite observation time. As validation metrics,
343 Pearson's correlation coefficient, median bias error (MBE), the fraction (%) within the
344 expected error of MODIS DT (EE), and Global Climate Observing System requirement for
345 AOD (GCOS; GCOS, 2011) were applied. The accuracy requirement of GCOS for satellite-
346 derived AOD at 550nm is 10% or 0.03, whichever is larger. The EE provided by the MODIS
347 DT algorithm (EE as $\pm 0.05 \pm 0.15 \times \text{AOD}$; (Levy et al., 2010)) was used for consistent
348 comparison with previous studies.

349 Table 2 shows the validation metrics of the respective product during the two field
350 campaigns. The collocation points for validation with AERONET of two AHI and two GOCI
351 products were not significantly different. %EE and %GCOS of AES and AMR showed better
352 accuracy than GV1 and GV2 during the KORUS and the EMeRGe periods. In terms of MBE,
353 GV2 is 0.008 and -0.001, which shows during the KORUS-AQ and the EMeRGe periods
354 close to zero. Additionally, further analyzes of the respective satellite product are carried out
355 along with fused products in Section 5.

357 4. Results

358 Figure 4 (a) shows the average AOD of FM1 (MLE method with all products) during the
359 KORUS-AQ period, and Figure 4 (b-e) shows the respective difference of the average AOD
360 of AMR, AES, GV1, and GV2 with respect to FM1. FM1 was selected as the representative
361 fused product as FM1 used all four satellite-derived products for fusion with bias correction.
362 The result of the comparison with the respective satellite product (Figure 4 (b-e)) shows
363 different features. AMR shows a negative bias over the ocean but shows similar results to
364 FM1 over land, while AES shows a different tendency in northern and southern China. GV1
365 tends to show opposite pattern to AES, and GV2 shows positive bias over the ocean and
366 results in similar pattern to FM1 over the land. In the west of the Korean peninsula, AES
367 AOD has a positive offset compared to FM1. Although the AES algorithm considers the
368 fraction of urbanization, there is still a tendency to have a positive AOD offsets. The main
369 reason why AES results show different patterns is the different estimation process of the land
370 surface reflectance from that of other products.

371 On the other hand, in GV1, the AOD over the Manchurian region has a positive offset
372 compared to FM1. This is because the aerosol signal is small over bright surface, making it
373 difficult to retrieve aerosol properties. These features tend to be alleviated in GV2, where the
374 surface reflectance and cloud removal process were improved.

375 Figure 5 shows the same result as Figure 4 except for the EMeRGe period. The AMR and
376 AES AODs appeared high in northern China, which is thought to be the snow contaminated
377 pixel. The EMeRGe period was in March-April, when northern China is more covered by
378 snow compared to the KORUS-AQ period in May-June. On the other hand, for GV1 and
379 GV2, the effect of overestimation with snow contaminated pixel is relatively small, as their
380 snow masking is well performed. However, for the KORUS-AQ period, it seems that the
381 GV1's overestimation of AOD in northern China still remains. Since this analysis (Figure 4
382 and 5) is for the fusion between the three MRM results and one ESR result, the average field
383 difference is naturally the largest in AES which uses ESR method.

384 For the characteristics of the average AOD for the two campaign period, high AODs during
385 the KORUS-AQ period were found in eastern China, and Hokkaido as wildfires from Russia
386 were transported to Hokkaido (Lee et al., 2019). Meanwhile, during the EMeRGe period,
387 high AOD is shown over the Yellow sea as aerosols were transported from China to the
388 Korean peninsula through the west coast, contrary to the KORUS-AQ period. Overall, the
389 average AODs for the EMeRGe are less smooth than those of the KORUS-AQ period. This is
390 because the EMeRGe period was shorter than that of the KORUS-AQ, and the retrieval
391 accuracy was lower due to the bright surface.

392

393 5. Validation, comparison, and error estimation against AERONET

394 5.1 Validation for fused AOD products with AERONET

395

396 The spatio-temporal matching method between fused AOD and AERONET was performed
397 as mentioned above in Section 3.5, and the statistics indices used for verification are also the
398 same. Validation indices of fused products with AERONET AOD during the two campaign

399 periods are summarized in Table 3. During the KORUS-AQ, fused AODs have better
400 accuracy of than respective satellite product in terms of %EE and %GCOS. The %EE
401 and %GCOS of AES, which showed the best accuracy among the respective product, are 63.5%
402 and 43.6%, which are poor than the worst accuracy of the fused AOD. All RMSE has been
403 improved except for FM2. The RMSE of FM2 is higher than RMSE of respective satellite
404 product by 0.001. Although all MBEs show different patterns, the deviation of the fused
405 products tends to be smaller. GV2 and F2 show MBE of 0.008, close to zero.

406 Next, %EE for the EMeRGe period exceeded 60.0, with AMR having the best accuracy of
407 69.4. Likewise, %GCOS was also the highest with 52.4, which showed better accuracy than
408 the fused product. In terms of MBE, GV2 was the best, with -0.001. The fused products did
409 not have the best statistical values, but they show overall better statistical values.

410 Figure 6 shows the %GCOS for the respective satellite product and fused products at each
411 validation site during each campaign. In Figure 6(a), for the KORUS period, F1 and FM1
412 show the highest % GCOS at 20 sites out of 35. Other than the fused result, AES shows the
413 highest %GCOS at 13 sites, which are mostly dense vegetation-area and coastal sites. On the
414 other hand, during EMeRGe period, the %GCOS of fused products was highest at 7 sites out
415 of 22, while respective satellite product showed at the rest of the sites in similar proportions.
416

417 **5.2 Error estimation**

418 Differences between satellite products and AERONET, dAOD values were analyzed in
419 terms of NDVI and observation times (Figure 7). Figure 7 (a) and (d) shows the respective
420 satellite product, Figure 7 (b) and (e) the ensemble-mean product, and Figure 7 (c) and (f) the
421 MLE fusion results, with each filled circle representing the mean of 500 and 400 collocated
422 data points sorted in terms of NDVI for the KORUS-AQ and the EMeRGe campaigns,
423 respectively. Figure 7 (a) shows different biases for each satellite product, with AMR and
424 GV1 being negative, AES and GV2 being positive. The errors are close to zero for both the
425 ensemble-mean and MLE products except for FM2 as a result of the fusion process.
426 When the NDVI is small, the mean AOD bias for GV2 dAOD was close to zero, but when
427 the NDVI is large, the mean AOD bias was negative as shown in Figure 3. The bias
428 correction effect of GV2 shows a small effect for small NDVI bins and a large effect for large
429 NDVI bins. In fact, the collocated dAODs of FM2 show close to zero when the NDVI bins
430 are greater than 0.4 (in Figure 7 (a)).

431 During the EMeRGe campaign (right column, Figure 7), the two AHI and two GOCI
432 products show negative biases, and even the ensemble-mean results have negative biases. The
433 ensemble-mean does not include any bias correction, meaning that the error characteristics of
434 each original satellite product are intact. The MLE products display improved biases in terms
435 of NDVI, which are close to zero because the bias was corrected for in the MLE process.
436 During the EMeRGe period, the collocated dAOD values at NDVI around 0.1 have a
437 negative value for all satellite-derived products (especially AHI products), and GV1 has a
438 negative value for bins where NDVI is greater than 0.2. During the EMeRGe period, the
439 collocated dAOD values at NDVI around 0.1 show negative values for all respective product
440 (especially AHI products), and dAOD for GV1 shows negative values for NDVI bins greater
441 than 0.2. The fused products tend to have error close to zero except for F3 and FM3. In terms
442 of F3, the collocated dAOD value around 0.1 of the NDVI bin has negative values for both
443 AMR and AES, so the collocated dAOD of F3 remain negative. The mean AOD bias values
444 for FM3, AMR and AES (in Figure 3) are close to zero for NDVI at around 0.1, so the bias

445 correction effect is small. This can be explained by the fact that the collocated dAOD for
446 NDVI at around 0.2 during the EMeRGe period is closer to zero in FM3 than in F3.

447 The median bias of the AOD products over the observation time was analyzed as shown in
448 Figure 8 where the left column represents the KORUS-AQ and the right column the EMeRGe
449 campaign, with filled circles representing median values, and the error bar being ± 1 SD. As
450 in the KORUS-AQ campaign, the AMR shows a generally negative bias, as in the all-time
451 results, and a negative bias also exists in each time zone. In the AES, GV1, and GV2 case,
452 positive and negative biases appear differently according to time zones. The ± 1 SD of the
453 respective satellite product is larger at local noon and smaller at 00 and 07 UTC when SZA is
454 large. Fused products as shown in Figures 8 (b) and (c), have a smaller ± 1 SD, and the
455 collocated dAOD over the observation time is also close to zero. Meanwhile, FM2 shows the
456 same tendency of overestimation for the same reason as in the previous Figure 7(a).

457 For the EMeRGe period, the collocated dAOD values of the respective product appear
458 closer to zero than KORUS-AQ. Similarly, the collocated dAOD of the fused products also
459 show values close to zero.

460 The error analysis indicates that the results after fusion are more accurate than the results
461 obtained using individual satellite product, and fused products accuracy was slightly better
462 during KORUS-AQ than EMeRGe because more data points were considered. Also, the
463 surface was relatively dark during the KORUS-AQ period, thus reduced errors for aerosol
464 retrieval than during the EMeRGe period.

465 **5.3 Time-series analysis of daily mean and hourly AODs**

466 The Gangneung-Wonju National University site (Gangneung-WNU; 128.87°E, 37.77°N)
467 lies on the eastern side of the Korean Peninsula and it is one of the regions with low aerosol
468 loadings. The AOD frequency distribution generally follows a log-normal distribution, and it
469 is important to evaluate accuracy for low AOD values. Therefore, we evaluated whether the
470 fused products were improved at low AODs. A daily mean time-series and diurnal variation
471 comparison of different satellite AOD products against AERONET (on a logarithmic scale)
472 are shown in Figure 9 for the Gangneung-WNU site without high AOD events, where most
473 point AERONET AODs at 550 nm were < 1 during the KORUS-AQ campaign. Daily mean
474 time-series data from the AERONET, ensemble-mean, and MLE products are shown in
475 Figure 9 (a-c), where black filled circles and black error bar represent AERONET AOD and
476 ± 1 SD of one-day average AERONET AOD. Satellite-derived AODs represented in different
477 colors show similar variabilities.

478 Respective satellite product generally shows similar daily-mean AOD distribution to
479 AERONET AOD. AMR, GV1, GV2 using MRM technique show similar patterns, and AES
480 using SWIR for surface reflectance estimation shows different patterns. The daily-mean AOD
481 of AES is more close to AERONET. On the other hand, Figure 9 (b) and (c) representing
482 fused AOD show similar patterns overall, but the daily-mean AODs on 11 May show
483 different patterns. Here, ensemble-mean products (F1-4) are less accurate than an individual
484 AES product, while MLE products (FM1-3) exhibit similar diurnal variation to daily-mean
485 AERONET AOD. To further analyze this, the daily-mean AOD is shown in Figure 9 (d-f)
486 instead of the hourly AOD for 11- 14 May.

487 As in the previous daily-mean AOD results, Figure 9 (d) shows the hourly AES AOD
488 variations are close to hourly AERONET, while AMR, GV1, and GV2 tend to underestimate.
489 Similarly, as shown in Figure 9 (e), hourly AOD variation of the ensemble-mean products
490 shows overall underestimation for 11 May. All ensemble-mean products use AES as an
491 ensemble member, but do not sufficiently compensate for the negative biases held by AMR,

492 GV1, and GV2. Meanwhile, MLE fused products show similar patterns to the hourly AOD
493 variation of AERONET, such as AES outputs. This can be explained in two ways: the effect
494 of considering the weighted function based on pixel-level uncertainty (RMSE in this study)
495 and the bias correction effects. Figure 1 showed similar RMSE values for all observation
496 times when $AOD \leq 0.5$. Gangneung-WNU site is one of the densely vegetated areas, but if
497 the AOD is less or equal to 0.5, there is little sensitivity of RMSE according to NDVI bins.
498 That is, regardless of the NDVI, each satellite-specific weighting function used for the MLE
499 fusion has a similar value for all satellite-derived products. The difference between the
500 ensemble-mean and the MLE fused products is due to the bias correction considered in the
501 MLE fusion. For example, the FM3 states that AMR has a large negative bias in the
502 afternoon and AES has a negative bias in the morning. With the bias correction of AES and
503 AMR respectively in the morning and afternoon, FM3 is calibrated in a direction to
504 compensate the underestimated AOD. The effect of bias correction and MLE fusion
505 agreement varies depending on the NDVI and AOD loading for each pixel. If bias correction
506 was not performed in the case on 11 May, the MLE fusion output shows very similar values
507 to F3.

508 The MLE products were implemented in a way to improve accuracy for the low AOD
509 region more critically than in the high AOD region by systematic bias correction. In general
510 surface reflectance estimated by the MRM is affected by BAOD, to result in a negative bias
511 in AOD. On the other hand, the AES uses TOA reflectance at 1.6 μm wavelength to estimate
512 surface reflectance and is therefore less affected by BAOD, and shows higher AOD than
513 AMR and the two GOCI AODs. Furthermore, AOD retrieval over vegetated areas is more
514 accurate with the ESR method. This result is consistent with previous studies of aerosol
515 retrieval in the VIS region (Levy et al., 2013; Gupta et al., 2019; Hsu et al., 2019).
516

517 **5.4 Accuracy evaluation for AHI products of the outside of GOCI domain**

518 In this section, the AMR, AES, F3, and FM3 products were evaluated at 34 sites within the
519 0-50°N and 70-150°E except for the GOCI domain as shown in Figures 4 and 5 (112-148°E,
520 24-50°N). The evaluation results are summarized in Table 4 in terms of N, R, RMSE, MBE,
521 and GCOS fraction. The RMSE and mean AOD bias values within the GOCI domain were
522 used in the MLE fusion in this section (see Figures 1 and 3). Table 4 shows the %GCOS and
523 RMSE values with poor accuracy than the validation results for the GOCI coverage as listed
524 in Table 4. In addition, BME during the KORUS-AQ and the EMeRGe period was -0.098
525 and -0.135 for AMR, and 0.130 and -0.055 for AES, respectively, which show very poor
526 accuracy. This can be explained by the cloud contamination issue at sites near the equator,
527 including Thailand. In addition, since AMR cannot collect enough clear pixels for the
528 estimation of LER, which can cause errors. Furthermore, MRM does not work well over
529 desert areas. On the other hand, AES has issues with poor accuracy over bright pixels such as
530 desert and snow contaminated areas. Second, there are many areas where the coastline is
531 complex as in Hong Kong, and the surface elevation is uneven as in Himalayas. However,
532 there is a bias of -0.055 during the EMeRGe period for AES, but the %GCOS was the highest
533 with 34.1, which is considered significant. F3 and FM3 show similar patterns for the
534 KORUS-AQ and the EMeRGe period. The accuracy of F3 is better than that of FM3, because
535 the previously mentioned issue for the bias correction has worked incorrectly, as the RMSE
536 and bias correction values used were from the data in the untrained area.
537

538 6. Summary and conclusion

539 Various aerosol algorithms have been developed for two different GEO satellites, AHI and
540 GOCI. Retrieved AOD data have advantages and disadvantages, depending on the concept of
541 the algorithm and surface-reflectance estimations. In this study, four aerosol products (GV1,
542 GV2, AMR, and AES) were used to construct ensemble-mean and MLE products. For the
543 ensemble-mean, this study presented fusion products taking advantage of overlap region,
544 accuracy, and near-real-time processing. For MLE products, bias corrections for different
545 observation times and surface type were performed considering pixel-level errors, and the
546 synergy of fusion between GEO satellites was successfully demonstrated.

547 Validation with the AERONET confirmed that averaging ensemble members improved
548 most of statistical metrics for ensemble products, and consideration of pixel-level uncertainty
549 further improved the accuracy of MLE products. For optimized AOD products in East Asia,
550 NDVI and time-dependent errors have been reduced. The ensemble-mean and MLE fusion
551 results show consistent results with better accuracy.

552 By comparing F1 and F4, we can see the accuracy changes depending on the number of
553 members used in the ensemble-mean. During the KORUS-AQ period, poor accuracy of each
554 member for ensemble averaging made difficult to find true features. The accuracy of F4 was
555 higher than that of F1, which shows the effect of GV1's large bias during the KORUS-AQ
556 period. On the other hand, for the EMERGe period, the difference between F1 and F4 appears
557 small because the respective ensemble member's accuracy was better. Both near-real-time
558 products, F2 and FM2, show good accuracy, similar to other fused products. Interestingly, the
559 accuracy of F1 was worse than that of F2, but the accuracy of FM1 was better than that of
560 FM2. The reason for this appears that the long-term RMSE (in Figure 1) and mean AOD bias
561 value (in Figure 3) was a better representation for the EMERGe than for the KORUS-AQ
562 period. To minimize such errors, overall results can be improved by binning the RMSE and
563 mean AOD bias value for the bias correction with respect to month and season in addition to
564 NDVI and time. Naturally, if we directly use the RMSE and mean AOD center value of each
565 campaign, the accuracy can be improved.

566 In terms of %GCOS range, satellite-derived and fused products was 33-43% and 46-54%,
567 respectively during the KORUS-AQ, indicating that the fused products have a better or
568 similar statistical score along with other validation scores such as RMSE and MBE. However,
569 the %GCOS during the EMERGe period shows better accuracy for AMR products with 52.4%
570 than for fused products with a maximum of 47.6%. In terms of other validation indices,
571 however, such as RMSE and MBE, the fused product results represent a better validation
572 score than the AMR. For low aerosol loading case where RMSE is small and similar across
573 different products, bias correction effect was also analyzed at the Gangneung-WNU site by
574 comparing F3 and FM3.

575 As a summary, to increase the accuracy of the fused products, it is required to have either
576 high accuracy of the respective satellite product, or the consistent error characteristics with
577 respect to different parameters such as time, NDVI, etc. If either each satellite-derived AOD
578 is accurate or large numbers of ensemble members are available for compensating respective
579 error, the ensemble-mean shall be the better fusion technique. If the error characteristic is not
580 random and can be expressed as a specific function, the fused product's accuracy through the
581 MLE fusion will be increased.

582 The method applied in this study could be used for AOD fusion of GEO data, such as AMI
583 onboard GK-2A, GOCI-2 and GEMS onboard GK-2B. Furthermore, it is possible to retrieve
584 AOPs other than AOD using multi-angle and multi-channel (UV, VIS, and IR) observations
585 with GK-2A and 2B.

586
587
588
589
590
591
592
593
594
595
596
597
598
599
600
601
602
603
604

Code and data availability.

The aerosol products data from AHI and GOCI are available on request from the corresponding author (jkim2@yonsei.ac.kr).

Author contributions.

HL, SG and JK designed the experiment. HL and SG carried out the data processing. MC, SL, and YK provided support on satellite data. HL wrote the manuscript with contributions from co-authors. JK reviewed and edited the article. JK and CK provided support and supervision. All authors analyzed the measurement data and prepared the article with contributions from all co-authors.

Competing interests.

The authors declare that they have no conflict of interest.

Acknowledgements

We thank all principal investigators and their staff for establishing and maintaining the AERONET sites used in this investigation. This subject is supported by Korea Ministry of Environment (MOE) as "Public Technology Program based on Environmental Policy (2017000160001)". This work was also supported by a grant from the National Institute of Environment Research (NIER), funded by the Ministry of Environment (MOE) of the Republic of Korea (NIER-2021-01-02-071). This work was also supported by a grant from the NIER, funded by the MOE of the Republic of Korea (NIER-2021-04-02-056). This research was also supported by the FRIEND (Fine Particle Research Initiative in East Asia Considering National Differences) Project through the National Research Foundation of Korea (NRF) funded by the Ministry of Science and ICT (Grant No.: 2020M3G1A1114615). We thank all members of the KORUS-AQ science team for their contributions to the field study and the data processing (doi:10.5067/Suborbital/KORUSAQ/DATA01).

References

Bernard, E., Moulin, C., Ramon, D., Jolivet, D., Riedi, J., and Nicolas, J. M.: Description and validation of an AOT product over land at the 0.6 μm channel of the SEVIRI sensor onboard MSG, *Atmospheric Measurement Techniques*, 4, 2543-2565, 2011.

Bessho, K., Date, K., Hayashi, M., Ikeda, A., Imai, T., Inoue, H., Kumagai, Y., Miyakawa, T., Murata, H., Ohno, T., Okuyama, A., Oyama, R., Sasaki, Y., Shimazu, Y., Shimoji, K., Sumida, Y., Suzuki, M., Taniguchi, H., Tsuchiyama, H., Uesawa, D., Yokota, H., and Yoshida, R.: An Introduction to Himawari-8/9—Japan's New-Generation Geostationary Meteorological Satellites, *Journal of the Meteorological Society of Japan*. Ser. II, 94, 151-183, 2016.

Bilal, M., Nichol, J. E., and Wang, L.: New customized methods for improvement of the MODIS C6 Dark Target and Deep Blue merged aerosol product, *Remote Sensing of Environment*, 197, 115-124, 2017.

630 Chatterjee, A., Michalak, A. M., Kahn, R. A., Paradise, S. R., Braverman, A. J., and Miller, C. E.: A
631 geostatistical data fusion technique for merging remote sensing and ground-based observations of aerosol
632 optical thickness, *Journal of Geophysical Research*, 115, 2010.

633 Cho, Hi K., Jeong, M. J., Kim, J., Kim, Y. J.: Dependence of diffuse photosynthetically active solar irradiance
634 on total optical depth, *Journal of Geophysical Research*, 108, D9, 4267, 4-1~4-10, 2003.

635
636 Choi, J.-K., Park, Y. J., Ahn, J. H., Lim, H.-S., Eom, J., and Ryu, J.-H.: GOCI, the world's first geostationary
637 ocean color observation satellite, for the monitoring of temporal variability in coastal water turbidity, *Journal of*
638 *Geophysical Research: Oceans*, 117, C9, 2012.

639 Choi, M., Kim, J., Lee, J., Kim, M., Park, Y.-J., Jeong, U., Kim, W., Hong, H., Holben, B. N., Eck, T. F., Song,
640 C. H., Lim, J.-H., and Song, C.-K.: GOCI Yonsei Aerosol Retrieval (YAER) algorithm and validation during
641 the DRAGON-NE Asia 2012 campaign, *Atmos. Meas. Tech.*, 9, 1377-1398, 2016.

642 Choi, M., Kim, J., Lee, J., Kim, M., Park, Y.-J., Holben, B., Eck, T. F., Li, Z., and Song, C. H.: GOCI Yonsei
643 aerosol retrieval version 2 products: an improved algorithm and error analysis with uncertainty estimation from
644 5-year validation over East Asia, *Atmospheric Measurement Techniques*, 11, 385-408, 2018.

645 Cox, C.: Statistics of the sea surface derived from sun glitter, *J. Marine Research*, 13, 198-227, 1954.

646 Crawford, J., J.-Y. Ahn, J. Al-Saadi, L. Chang, L. K. Emmons, J. Kim, G. Lee, J.-H. Park, R. J. Park, J. H. Woo,
647 C.-K. Song, J.-H. Hong, Y.-D. Hong, B. L. Lefer, M. Lee, T. Lee, S. Kim, K.-E. Min, S. S. Yum, H. J. Shin, Y.-
648 W. Kim, J.-S. Choi, J.-S. Park, J. J. Szykman, R. W. Long, C. E. Jordan, I. J. Simpson, A. Fried, J. E. Dibb, S. Y.
649 Cho, and Y. P. Kim: The Korea-United States Air Quality (KORUS-AQ) Field Study, *Elementa*, revised, 2021

650
651 Fukuda, S., Nakajima, T., Takenaka, H., Higurashi, A., Kikuchi, N., Nakajima, T. Y., and Ishida, H.: New
652 approaches to removing cloud shadows and evaluating the 380 nm surface reflectance for improved aerosol
653 optical thickness retrievals from the GOSAT/TANSO-Cloud and Aerosol Imager, *Journal of Geophysical*
654 *Research: Atmospheres*, 118, 13, 520-513, 531, 2013.

655 Garay, M. J., Kalashnikova, O. V., and Bull, M. A.: Development and assessment of a higher-spatial-resolution
656 (4.4 km) MISR aerosol optical depth product using AERONET-DRAGON data, *Atmospheric Chemistry and*
657 *Physics*, 17, 5095-5106, 2017.

658 Garay, M. J., Witek, M. L., Kahn, R. A., Seidel, F. C., Limbacher, J. A., Bull, M. A., Diner, D. J., Hansen, E. G.,
659 Kalashnikova, O. V., Lee, H., Nastan, A. M., and Yu, Y.: Introducing the 4.4Ékm spatial resolution
660 Multi-Angle Imaging SpectroRadiometer (MISR) aerosol product, *Atmospheric Measurement Techniques*, 13,
661 593-628, 2020.

662 GCOS, W.: Systematic Observation Requirements for Satellite-BASED Data Products for Climate, 154
663 Document. 2011.

664
665 Giles, D. M., Sinyuk, A., Sorokin, M. S., Schafer, J. S., Smirnov, A., Slutsker, I., Eck, T. F., Holben, B. N.,
666 Lewis, J., Campbell, J., Welton, E. J., Korkin, S., and Lyapustin, A.: Advancements in the Aerosol Robotic
667 Network (AERONET) Version 3 Database – Automated Near Real-Time Quality Control Algorithm with
668 Improved Cloud Screening for Sun Photometer Aerosol Optical Depth (AOD) Measurements, *Atmos. Meas.*
669 *Tech. Discuss.*, doi: <https://doi.org/10.5194/amt-2018-272>, 2018. 2018.

670 Go, S., Kim, J., Park, S. S., Kim, M., Lim, H., Kim, J.-Y., Lee, D.-W., and Im, J.: Synergistic Use of
671 Hyperspectral UV-Visible OMI and Broadband Meteorological Imager MODIS Data for a Merged Aerosol
672 Product, *Remote Sensing*, 12, 2020.

673
674 Gupta, P., Patadia, F., and Christopher, S. A.: Multisensor Data Product Fusion for Aerosol Research, *IEEE*
675 *Transactions on Geoscience and Remote Sensing*, 46, 1407-1415, 2008.

676 Gupta, P., Levy, R. C., Mattoo, S., Remer, L. A., and Munchak, L. A.: A surface reflectance scheme for
677 retrieving aerosol optical depth over urban surfaces in MODIS Dark Target retrieval algorithm, *Atmospheric*
678 *Measurement Techniques*, 9, 3293-3308, 2016.

- 679 Gupta, P., Levy, R. C., Mattoo, S., Remer, L. A., Holz, R. E., and Heidinger, A. K.: Applying the Dark Target
680 aerosol algorithm with Advanced Himawari Imager observations during the KORUS-AQ field campaign, 2019.
681 2019.
- 682 Herman, J., Bhartia, P., Torres, O., Hsu, C., Seftor, C., and Celarier, E.: Global distribution of UV-absorbing
683 aerosols from Nimbus 7/TOMS data, *Journal of Geophysical Research: Atmospheres*, 102, 16911-16922, 1997.
- 684 Holben, B. N., Tanre, D., Smirnov, A., Eck, T., Slutsker, I., Abuhassan, N., Newcomb, W., Schafer, J., Chatenet,
685 B., and Lavenu, F. J. J. o. G. R. A.: An emerging ground-based aerosol climatology: Aerosol optical depth from
686 AERONET, 106, 12067-12097, 2001.
- 687 Hsu, N. C., Tsay, S.-C., King, M. D., Herman, J. R. J. I. T. o. G., and Sensing, R.: Aerosol properties over
688 bright-reflecting source regions, 42, 557-569, 2004.
- 689 Hsu, N., Jeong, M. J., Bettenhausen, C., Sayer, A., Hansell, R., Seftor, C., Huang, J., and Tsay, S. C.: Enhanced
690 Deep Blue aerosol retrieval algorithm: The second generation, *Journal of Geophysical Research: Atmospheres*,
691 118, 9296-9315, 2013.
- 692 Hsu, N., Lee, J., Sayer, A., Kim, W., Bettenhausen, C., and Tsay, S. C. J. J. o. G. R. A.: VIIRS Deep Blue
693 aerosol products over land: Extending the EOS long-term aerosol data records, 124, 4026-4053, 2019.
- 694 Jackson, J. M., Liu, H., Laszlo, I., Kondragunta, S., Remer, L. A., Huang, J., and Huang, H.-C.: Suomi-NPP
695 VIIRS aerosol algorithms and data products, *Journal of Geophysical Research: Atmospheres*, 118, 12,673-
696 612,689, 2013.
- 697 Kikuchi, M., Murakami, H., Suzuki, K., Nagao, T. M., and Higurashi, A.: Improved Hourly Estimates of
698 Aerosol Optical Thickness Using Spatiotemporal Variability Derived From Himawari-8 Geostationary Satellite,
699 *IEEE Transactions on Geoscience and Remote Sensing*, 56, 3442-3455, 2018.
- 700 Kim, J., Lee, J., Lee, H. C., Higurashi, A., Takemura, T., and Song, C. H., Consistency of the aerosol type
701 classification from satellite remote sensing during the Atmospheric Brown Cloud–East Asia Regional
702 Experiment campaign, *J. Geophys. Res.*, 112, D22S33, doi:10.1029/2006JD008201, 2007.
- 703 Kim, J., Yoon, J. M., Ahn, M. H., Sohn, B. J., and Lim, H. S.: Retrieving aerosol optical depth using visible and
704 mid-IR channels from geostationary satellite MTSAT-1R, *International Journal of Remote Sensing*, 29, 6181-
705 6192, 2008.
- 706 Kim, J., Kim, M., and Choi, M.: Monitoring aerosol properties in east Asia from geostationary orbit: GOCI, MI
707 and GEMS. In: *Air Pollution in Eastern Asia: An Integrated Perspective*, Springer, 2017.
- 708 Kim, J., Jeong, U., Ahn, M.-H., Kim, J. H., Park, R. J., Lee, H., Song, C. H., Choi, Y.-S., Lee, K.-H., Yoo, J.-M.,
709 Jeong, M.-J., Park, S. K., Lee, K.-M., Song, C.-K., Kim, S.-W., Kim, Y. J., Kim, S.-W., Kim, M., Go, S., Liu,
710 X., Chance, K., Chan Miller, C., Al-Saadi, J., Veihelmann, B., Bhartia, P. K., Torres, O., Abad, G. G., Haffner,
711 D. P., Ko, D. H., Lee, S. H., Woo, J.-H., Chong, H., Park, S. S., Nicks, D., Choi, W. J., Moon, K.-J., Cho, A.,
712 Yoon, J., Kim, S.-k., Hong, H., Lee, K., Lee, H., Lee, S., Choi, M., Veeffkind, P., Levelt, P. F., Edwards, D. P.,
713 Kang, M., Eo, M., Bak, J., Baek, K., Kwon, H.-A., Yang, J., Park, J., Han, K. M., Kim, B.-R., Shin, H.-W., Choi,
714 H., Lee, E., Chong, J., Cha, Y., Koo, J.-H., Irie, H., Hayashida, S., Kasai, Y., Kanaya, Y., Liu, C., Lin, J.,
715 Crawford, J. H., Carmichael, G. R., Newchurch, M. J., Lefer, B. L., Herman, J. R., Swap, R. J., Lau, A. K. H.,
716 Kurosu, T. P., Jaross, G., Ahlers, B., Dobber, M., McElroy, C. T., and Choi, Y.: New Era of Air Quality
717 Monitoring from Space: Geostationary Environment Monitoring Spectrometer (GEMS), *Bulletin of the
718 American Meteorological Society*, 101, E1-E22, 2020.
- 719 Kim, M., Kim, J., Wong, M. S., Yoon, J., Lee, J., Wu, D., Chan, P. W., Nichol, J. E., Chung, C.-Y., and Ou, M.-
720 L.: Improvement of aerosol optical depth retrieval over Hong Kong from a geostationary meteorological satellite
721 using critical reflectance with background optical depth correction, *Remote Sensing of Environment*, 142, 176-
722 187, 2014.
- 723 Kim, M., Kim, J., Jeong, U., Kim, W., Hong, H., Holben, B., Eck, T. F., Lim, J. H., Song, C. K., Lee, S., and
724 Chung, C. Y.: Aerosol optical properties derived from the DRAGON-NE Asia campaign, and implications for a
725 single-channel algorithm to retrieve aerosol optical depth in spring from Meteorological Imager (MI) on-board
726 the Communication, Ocean, and Meteorological Satellite (COMS), *Atmos. Chem. Phys.*, 16, 1789-1808, 2016.

- 727 Kim, M., Kim, S. H., Kim, W. V., Lee, Y. G., Kim, J., and Kafatos, M. C.: Assessment of Aerosol optical depth
728 under background and polluted conditions using AERONET and VIIRS datasets, *Atmospheric Environment*,
729 245, 2021.
- 730 Knapp, K. R., Frouin, R., Kondragunta, S., and Prados, A.: Toward aerosol optical depth retrievals over land
731 from GOES visible radiances: determining surface reflectance, *International Journal of Remote Sensing*, 26,
732 4097-4116, 2007.
- 733 Koelemeijer, R., De Haan, J., and Stammes, P.: A database of spectral surface reflectivity in the range 335–772
734 nm derived from 5.5 years of GOME observations, *Journal of Geophysical Research: Atmospheres*, 108, 2003.
- 735 Lee, J., Kim, J., Song, C. H., Ryu, J.-H., Ahn, Y.-H., and Song, C.: Algorithm for retrieval of aerosol optical
736 properties over the ocean from the Geostationary Ocean Color Imager, *Remote Sensing of Environment*, 114,
737 1077-1088, 2010.
- 738 Lee, J., Kim, J., Yang, P., and Hsu, N. C.: Improvement of aerosol optical depth retrieval from MODIS spectral
739 reflectance over the global ocean using new aerosol models archived from AERONET inversion data and tri-
740 axial ellipsoidal dust database, *Atmospheric Chemistry and Physics*, 12, 7087-7102, 2012.
- 741 Levy, R. C., Remer, L. A., Kleidman, R. G., Mattoo, S., Ichoku, C., Kahn, R., and Eck, T. F.: Global evaluation
742 of the Collection 5 MODIS dark-target aerosol products over land, *Atmospheric Chemistry and Physics*, 10,
743 10399-10420, 2010.
- 744 Levy, R. C., Mattoo, S., Munchak, L. A., Remer, L. A., Sayer, A. M., Patadia, F., and Hsu, N. C.: The
745 Collection 6 MODIS aerosol products over land and ocean, *Atmospheric Measurement Techniques*, 6, 2989-
746 3034, 2013.
- 747 Lee, S., Kim, M., Choi, M., Go, S., Kim, J., Kim, J.-H., Lim, H.-K., Jeong, U., Goo, T.-Y., Kuze, A., Shiomi, K.,
748 and Tatsuya, Y.: Aerosol Property Retrieval Algorithm over Northeast Asia from TANSO-CAI Measurements
749 Onboard GOSAT, *Remote Sensing*, 9, 2017.
- 750
751 Lee, S., Kim, J., Choi, M., Hong, J., Lim, H., Eck, T. F., Holben, B. N., Ahn, J.-Y., Kim, J., and Koo, J.-H.:
752 Analysis of long-range transboundary transport (LRTT) effect on Korean aerosol pollution during the KORUS-
753 AQ campaign, *Atmospheric Environment*, 204, 53-67, 2019.
- 754
755 Li, L., Shi, R., Zhang, L., Zhang, J., and Gao, W.: The data fusion of aerosol optical thickness using universal
756 kriging and stepwise regression in East China, 2014, 922112.
- 757 Lim, H., Choi, M., Kim, M., Kim, J., and Chan, P. W.: Retrieval and Validation of Aerosol Optical Properties
758 Using Japanese Next Generation Meteorological Satellite, Himawari-8, *Korean Journal of Remote Sensing*, 32,
759 681-691, 2016.
- 760 Lim, H., Choi, M., Kim, J., Kasai, Y., and Chan, P.: AHI/Himawari-8 Yonsei Aerosol Retrieval (YAER):
761 Algorithm, Validation and Merged Products, *Remote Sens.*, 10, 2018.
- 762 Lyapustin, A., Martonchik, J., Wang, Y., Laszlo, I., and Korkin, S.: Multiangle implementation of atmospheric
763 correction (MAIAC): 1. Radiative transfer basis and look-up tables, *Journal of Geophysical Research*, 116,
764 2011a.
- 765 Lyapustin, A., Wang, Y., Laszlo, I., Kahn, R., Korkin, S., Remer, L., Levy, R., and Reid, J. S.: Multiangle
766 implementation of atmospheric correction (MAIAC): 2. Aerosol algorithm, *Journal of Geophysical Research*,
767 116, 2011b.
- 768 Lyapustin, A., Wang, Y., Korkin, S., and Huang, D.: MODIS Collection 6 MAIAC algorithm, *Atmospheric
769 Measurement Techniques*, 11, 5741-5765, 2018.
- 770 M elin, F., Zibordi, G., and Djavidnia, S.: Development and validation of a technique for merging satellite
771 derived aerosol optical depth from SeaWiFS and MODIS, *Remote Sensing of Environment*, 108, 436-450, 2007.
- 772 Murakami, H.: Ocean color estimation by Himawari-8/AHI, 2016, 987810.

773 Negi, H. and Kokhanovsky, A. J. T. C.: Retrieval of snow albedo and grain size using reflectance measurements
774 in Himalayan basin, 5, 203, 2011.

775 Nguyen, H., Cressie, N., and Braverman, A.: Spatial Statistical Data Fusion for Remote Sensing Applications,
776 Journal of the American Statistical Association, 107, 1004-1018, 2012.

777 Nirala, M.: Technical Note: Multi-sensor data fusion of aerosol optical thickness, International Journal of
778 Remote Sensing, 29, 2127-2136, 2008.

779 Pang, J., Liu, Z., Wang, X., Bresch, J., Ban, J., Chen, D., and Kim, J.: Assimilating AOD retrievals from GOCI
780 and VIIRS to forecast surface PM2.5 episodes over Eastern China, Atmospheric Environment, 179, 288-304,
781 2018.

782 Remer, L. A., Kaufman, Y., Tanré, D., Mattoo, S., Chu, D., Martins, J. V., Li, R.-R., Ichoku, C., Levy, R., and
783 Kleidman, R.: The MODIS aerosol algorithm, products, and validation, Journal of the atmospheric sciences, 62,
784 947-973, 2005.

785 Remer, L. A., Mattoo, S., Levy, R. C., and Munchak, L.: MODIS 3 km aerosol product: algorithm and global
786 perspective, Atmospheric Measurement Techniques Discussions, 6, 69-112, 2013.

787 Saide, P. E., Kim, J., Song, C. H., Choi, M., Cheng, Y., and Carmichael, G. R.: Assimilation of next generation
788 geostationary aerosol optical depth retrievals to improve air quality simulations, Geophysical Research Letters,
789 41, 9188-9196, 2014.

790 Saide, P. E., Gao, M., Lu, Z., Goldberg, D., Streets, D. G., Woo, J.-H., Beyersdorf, A., Corr, C. A., Thornhill, K.
791 L., Anderson, B., Hair, J. W., Nehrir, A. R., Diskin, G. S., Jimenez, J. L., Nault, B. A., Campuzano-Jost, P.,
792 Dibb, J., Heim, E., Lamb, K. D., Schwarz, J. P., Perring, A. E., Kim, J., Choi, M., Holben, B., Pfister, G.,
793 Hodzic, A., Carmichael, G. R., Emmons, L., and Crawford, J. H. : Understanding and improving model
794 representation of aerosol optical properties for a Chinese haze event measured during KORUS-AQ,
795 Atmospheric Chemistry and Physics, 20, 6455-6478,2020.

796

797 Sayer, A., Munchak, L., Hsu, N., Levy, R., Bettenhausen, C., and Jeong, M. J.: MODIS Collection 6 aerosol
798 products: Comparison between Aqua's e-Deep Blue, Dark Target, and "merged" data sets, and usage
799 recommendations, Journal of Geophysical Research: Atmospheres, 119, 2014.

800 Sayer, A., Hsu, N., Lee, J., Bettenhausen, C., Kim, W., and Smirnov, A. J. J. o. G. R. A.: Satellite Ocean
801 Aerosol Retrieval (SOAR) Algorithm Extension to S-NPP VIIRS as Part of the "Deep Blue" Aerosol Project,
802 123, 380-400, 2018.

803 Sayer, A. M., Hsu, N. C., Lee, J., Kim, W. V., and Dutcher, S. T.: Validation, Stability, and Consistency of
804 MODIS Collection 6.1 and VIIRS Version 1 Deep Blue Aerosol Data Over Land, Journal of Geophysical
805 Research: Atmospheres, 124, 4658-4688, 2019.

806 Smirnov, A., Holben, B. N., Eck, T. F., Dubovik, O., and Slutsker, I.: Cloud screening and quality control
807 algorithms for the AERONET data base, Remote Sens. Environ., 73, 337-349, 2000.

808 Stocker, T. F., Qin, D., Plattner, G.-K., Tignor, M., Allen, S. K., Boschung, J., Nauels, A., Xia, Y., Bex, B., and
809 Midgley, B.: IPCC, 2013: climate change 2013: the physical science basis. Contribution of working group I to
810 the fifth assessment report of the intergovernmental panel on climate change. Cambridge University Press, 2013.

811 Tang, Q., Bo, Y., and Zhu, Y.: Spatiotemporal fusion of multiple-satellite aerosol optical depth (AOD) products
812 using Bayesian maximum entropy method, Journal of Geophysical Research: Atmospheres, 121, 4034-4048,
813 2016.

814 Wang, J.: Geostationary satellite retrievals of aerosol optical thickness during ACE-Asia, Journal of
815 Geophysical Research, 108, 2003.

816 Wang, J., Brown, D. G., and Hammerling, D.: Geostatistical inverse modeling for super-resolution mapping of
817 continuous spatial processes, Remote Sensing of Environment, 139, 205-215, 2013.

818 Wei, J., Li, Z., Sun, L., Peng, Y., and Wang, L.: Improved merge schemes for MODIS Collection 6.1 Dark
819 Target and Deep Blue combined aerosol products, *Atmospheric Environment*, 202, 315-327, 2019. Xie, Y., Xue,
820 Y., Che, Y., Guang, J., Mei, L., Voorhis, D., Fan, C., She, L., Xu, H. J. I. T. o. G., and Sensing, R.: Ensemble of
821 ESA/AATSR aerosol optical depth products based on the likelihood estimate method with uncertainties, 56,
822 997-1007, 2018.

823 Xu, H., Guang, J., Xue, Y., De Leeuw, G., Che, Y., Guo, J., He, X., and Wang, T. J. A. E.: A consistent aerosol
824 optical depth (AOD) dataset over mainland China by integration of several AOD products, 114, 48-56, 2015.

825 Xue, Y., Xu, H., Mei, L., Guang, J., Guo, J., Li, Y., Hou, T., Li, C., Yang, L., He, X. J. A. C., and Discussions,
826 P.: Merging aerosol optical depth data from multiple satellite missions to view agricultural biomass burning in
827 Central and East China, 12, 10461-10492, 2012.

828

829 Yoon, J. M., Kim, J., Lee, J. H., Cho, H. K., Sohn, B.-J., and Ahn, M.-H. J. A.-P. J. o. A. S.: Retrieval of aerosol
830 optical depth over East Asia from a geostationary satellite, *MTSAT-1R*, 43, 49-58, 2007.

831 Yoshida, M., Kikuchi, M., Nagao, T. M., Murakami, H., Nomaki, T., and Higurashi, A.: Common Retrieval of
832 Aerosol Properties for Imaging Satellite Sensors, *Journal of the Meteorological Society of Japan. Ser. II*, 96B,
833 193-209, 2018.

834 Zhong, G., Wang, X., Tani, H., Guo, M., Chittenden, A., Yin, S., Sun, Z., and Matsumura, S.: A Modified
835 Aerosol Free Vegetation Index Algorithm for Aerosol Optical Depth Retrieval Using GOSAT TANSO-CAI
836 Data, *Remote Sensing*, 8, 2016.

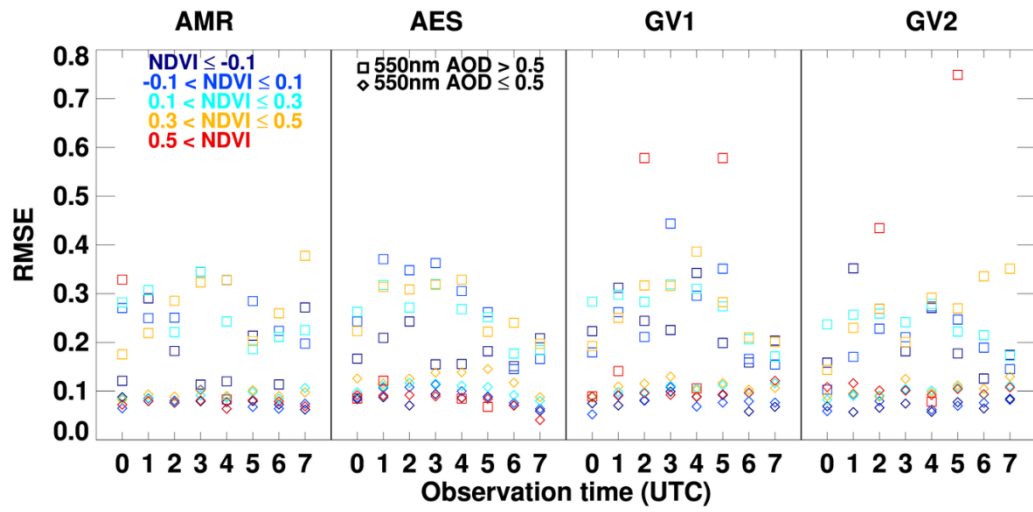
837

838 Table 1. Satellite dataset used for the fusion products. Four entries F1-F4, and three entries FM1-FM3 represent
 839 ensemble-mean fusion and MLE fusion products.

| AOD type | F1 | F2 | F3 | F4 | FM1 | FM2 | FM3 |
|----------|------------------------------|----------------------|-------------------------------|---|---------------------------|---------------|---------------|
| AER | o | o | o | o | o | o | o |
| AMR | o | | o | o | o | | o |
| GV1 | o | | | | o | | |
| GV2 | o | o | | o | o | o | |
| Remark | | | | Without GV1 to check missing effect | MLE Products ² | | |
| | All available products | For NRT ¹ | AHI only for wider area | | Same as F1 | Same as F2 | Same as F3 |

840 ¹NRT: near real time; ²Maximum Likelihood Estimation

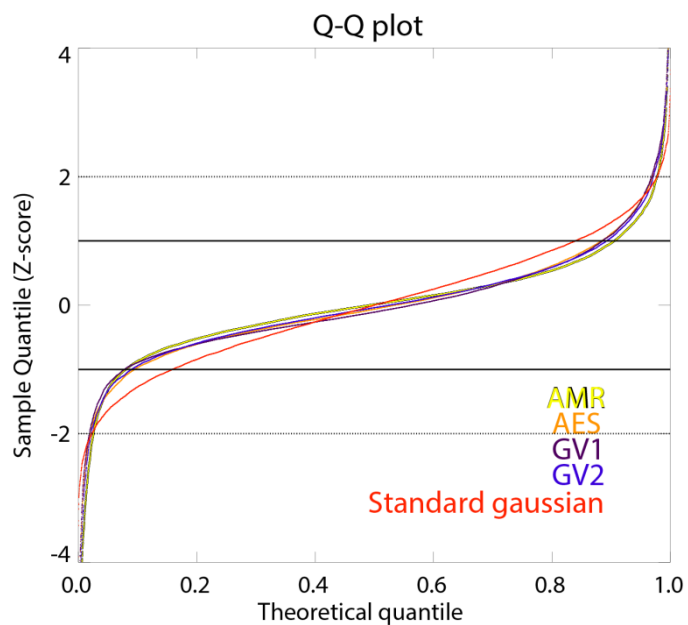
841



842
 843 Figure 1. RMSE according to NDVI (color), observation time, and satellite AODs (square and diamond
 844 represent AOD at 550nm greater and less equal than 0.5) during Apr. 2018 to Mar. 2019 excluding EMeRGe
 845 campaign. Colors represent different NDVI bins.

846

847

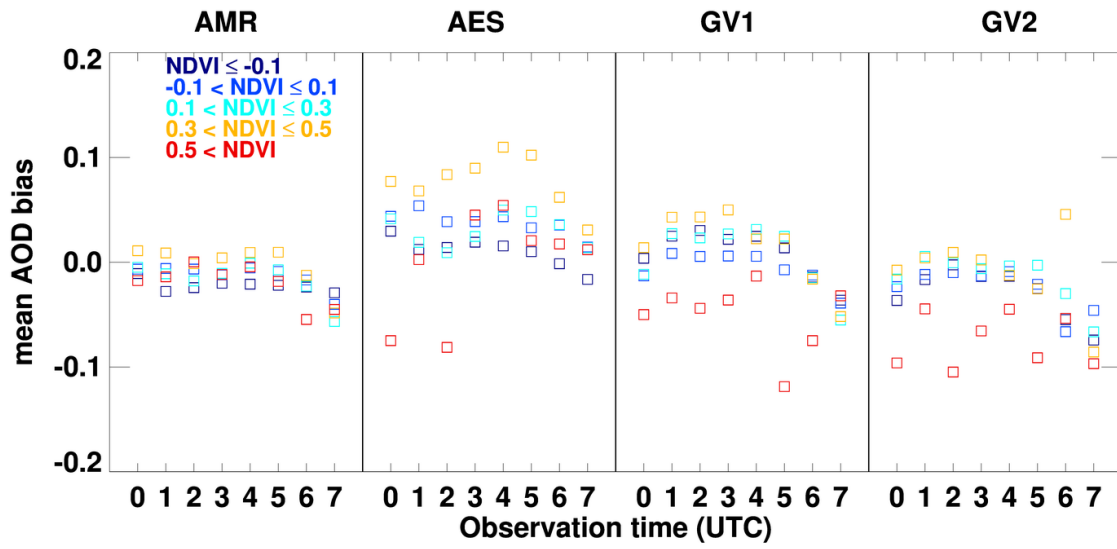


848
849
850

Figure 2. Q-Q plot for the difference between AERONET AOD and AMR(yellow), AES(orange), GV1(purple), and GV2(dark blue) AOD. The black solid line and dotted line represent 1- σ and 2- σ , respectively.

851

852



853

854 Figure 3. Systematic bias-correction values for NDVI groups and temporal bins for each satellite product from
855 Gaussian fitting analysis used in MLE fusion. Colors represent different NDVI bins.

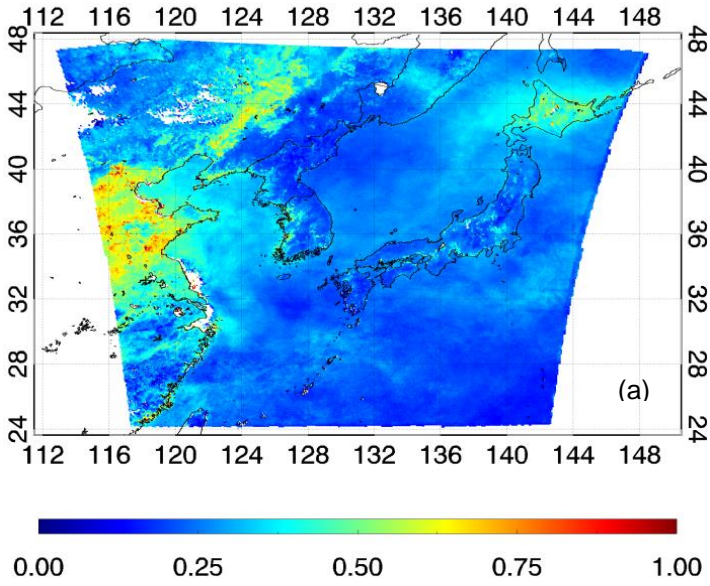
856

857 Table 2. Validation statistics of the respective satellite product during the KORUS-AQ and the EMerGe
 858 campaign.

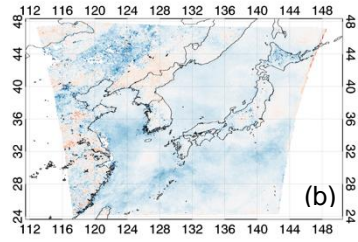
| Product type | KORUS-AQ | | | | | EMerGe | | | | |
|--------------|----------|-------|-------|--------|------|--------|-------|-------|--------|------|
| | %EE | %GCOS | RMSE | MBE | N | %EE | %GCOS | RMSE | MBE | N |
| AES | 63.5 | 43.6 | 0.145 | 0.029 | 5069 | 65.2 | 46.3 | 0.176 | -0.011 | 1884 |
| AMR | 60.6 | 39.4 | 0.150 | -0.054 | 5069 | 69.4 | 52.4 | 0.162 | -0.028 | 1884 |
| GV1 | 52.2 | 34.7 | 0.153 | -0.045 | 4843 | 63.4 | 42.7 | 0.162 | -0.035 | 1760 |
| GV2 | 50.3 | 33.8 | 0.176 | 0.008 | 4924 | 61.5 | 41.8 | 0.164 | -0.001 | 1863 |

859
 860

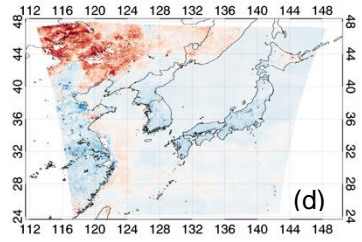
Mean FM1 AOD - KORUS-AQ



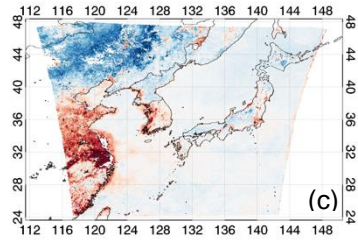
Difference between mean AMR & FM1 AOD - KORUS-AQ



Difference between mean GV1 & FM1 AOD - KORUS-AQ



Difference between mean AES & FM1 AOD - KORUS-AQ



Difference between mean GV2 & FM1 AOD - KORUS-AQ

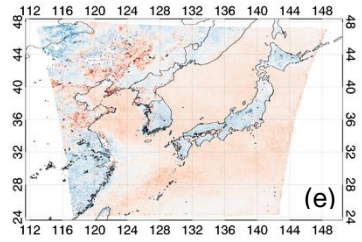


Figure 4. The average AOD of (a) FM1 (AMR, AES, GV1, and GV2) during the KORUS AQ. The difference of mean (b)AMR, (c)AES, (d) GV1, and (e) GV2 AODs with respect to mean representative (FM1) AOD. Figures generated with Interactive Data Language (IDL) version 8.8.0.

Mean FM1 AOD - EMeRGe

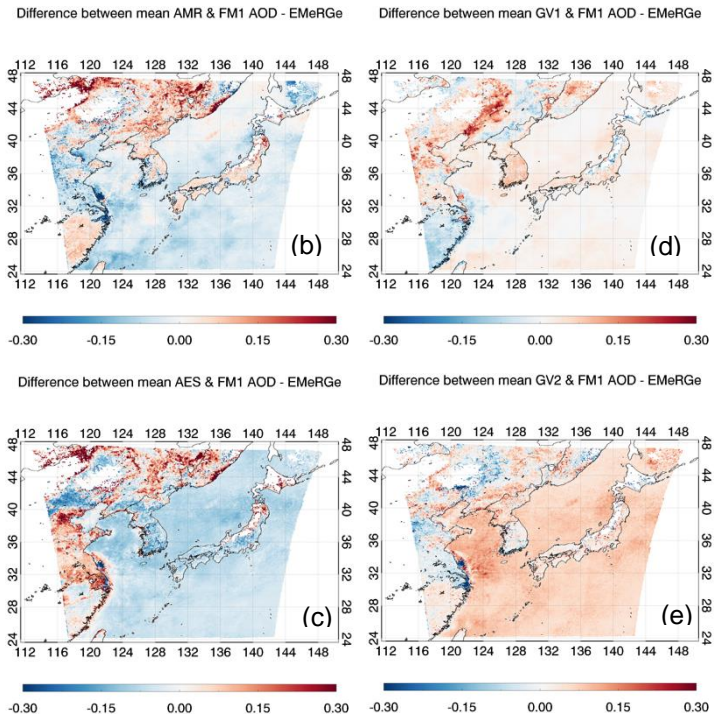
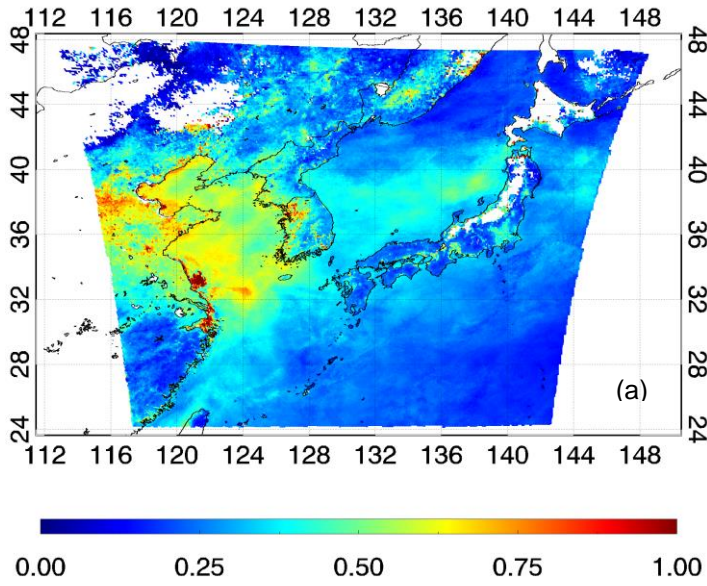


Figure 5. Same as Figure 4, but for EMeRGe campaign.

Table 3. Validation statistics of the ensemble-mean fusion (F1-F4), and MLE fusion (FM1-FM4) AOD during two field campaigns (left: KORUS-AQ, right: EMerGe).

| Fusion method | Product type | KORUS-AQ | | | | | EMerGe | | | | |
|---------------|--------------|----------|-------|-------|------------|------|--------|-------|-------|------------|------|
| | | %EE | %GCOS | RMSE | MBE | N | %EE | %GCOS | RMSE | MBE | N |
| Ensemble-mean | F1 | 67.8 | 47.2 | 0.134 | - 0.014 | 4806 | 66.8 | 45.4 | 0.149 | - 0.012 | 1754 |
| | F2 | 72.3 | 52.7 | 0.129 | 0.008 | 4843 | 66.9 | 45.5 | 0.150 | - 0.012 | 1760 |
| | F3 | 72.1 | 51.1 | 0.133 | 0.012 | 5069 | 63.2 | 44.5 | 0.175 | - 0.019 | 1884 |
| | F4 | 73.3 | 51.6 | 0.128 | - 0.015 | 4843 | 66.4 | 44.8 | 0.153 | - 0.024 | 1760 |
| MLE | FM1 | 72.6 | 52.4 | 0.130 | - 0.012 | 4806 | 69.1 | 47.6 | 0.147 | - 0.008 | 1754 |
| | FM2 | 65.5 | 46.1 | 0.146 | 0.034 | 4924 | 67.3 | 46.5 | 0.152 | 0.014 | 1863 |
| | FM3 | 75.2 | 54.5 | 0.129 | -0.09 | 5069 | 62.4 | 41.8 | 0.177 | - 0.027 | 1884 |

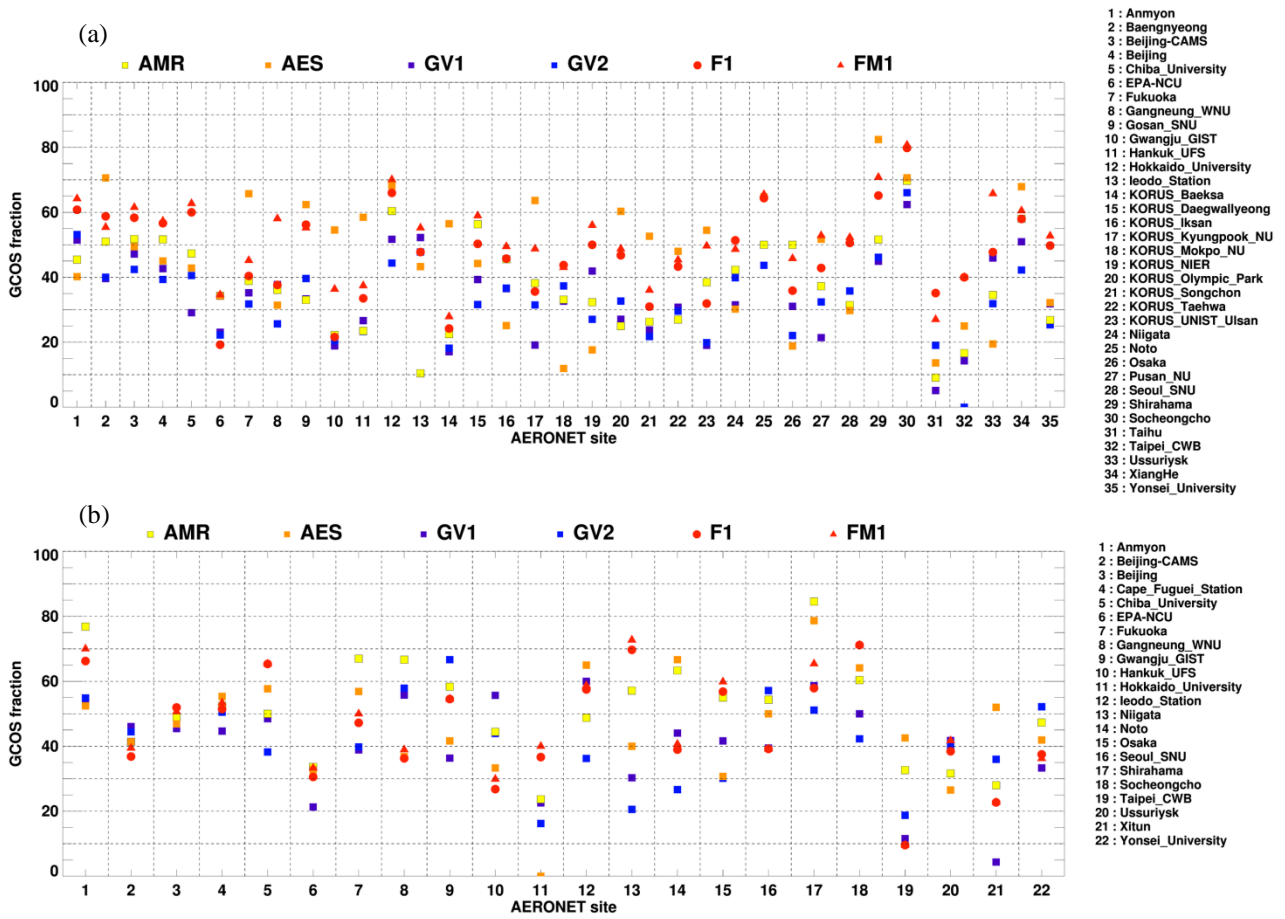


Figure 6. Comparison of the GCOS fraction for respective satellite (AMR, AES, GV1, and GV2), ensemble-mean fusion (F1), and MLE fusion (FM1) during the (a) KORUS-AQ and (b) EMerGe campaign. Colors represent different aerosol products.

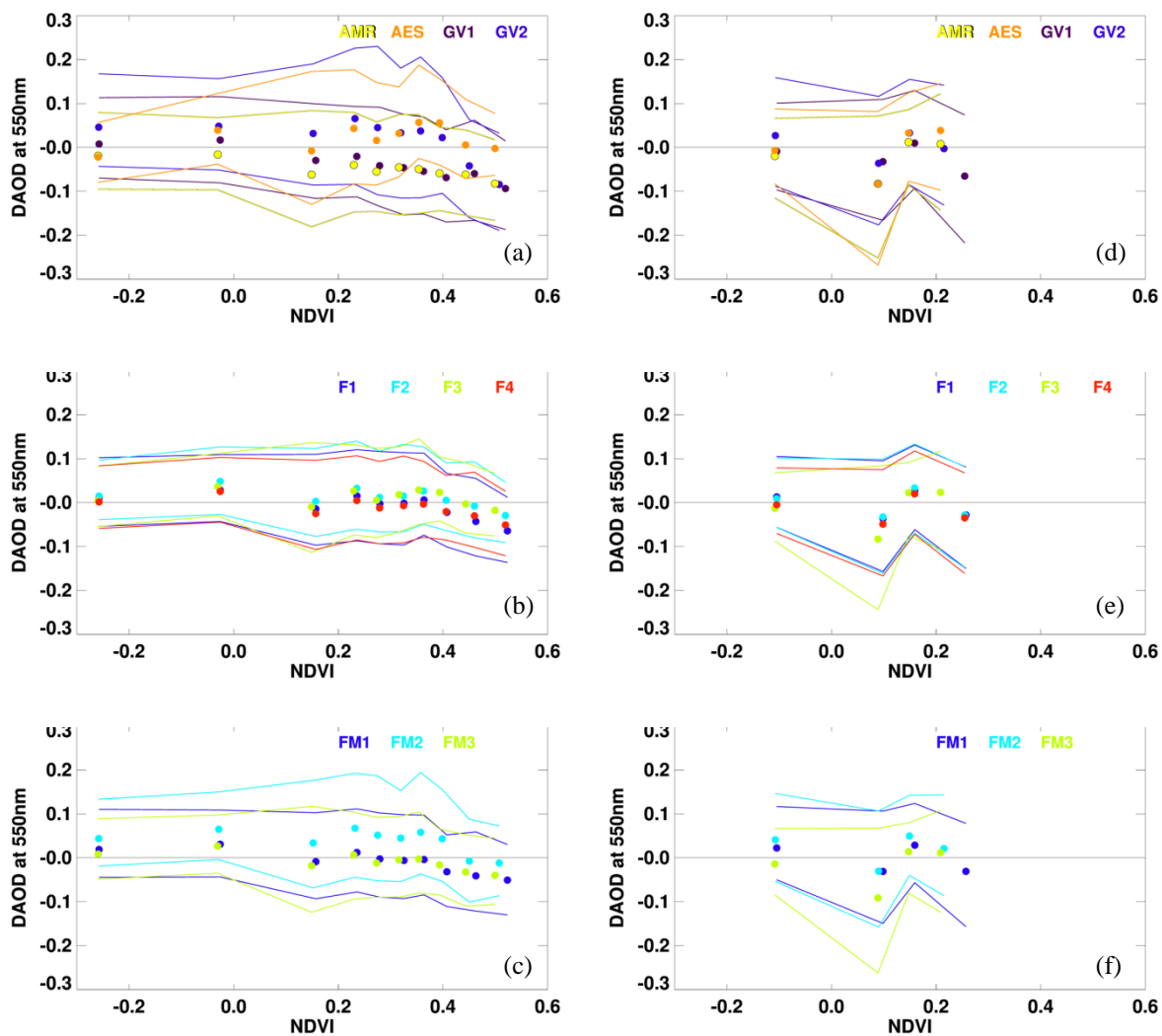


Figure 7. Difference between (a, d) respective, (b, e) ensemble-mean, or (c, f) MLE and AERONET AOD in terms of NDVI during the KORUS-AQ (left column) and the EMeRGe (right column) campaigns. Each points and solid lines represent the median and 1- σ (16th and 84th percentile) of 500 (for the KORUS-AQ) and 400 (for the EMeRGe) collocated data points in terms of NDVI values, respectively. Colors represent different aerosol products.

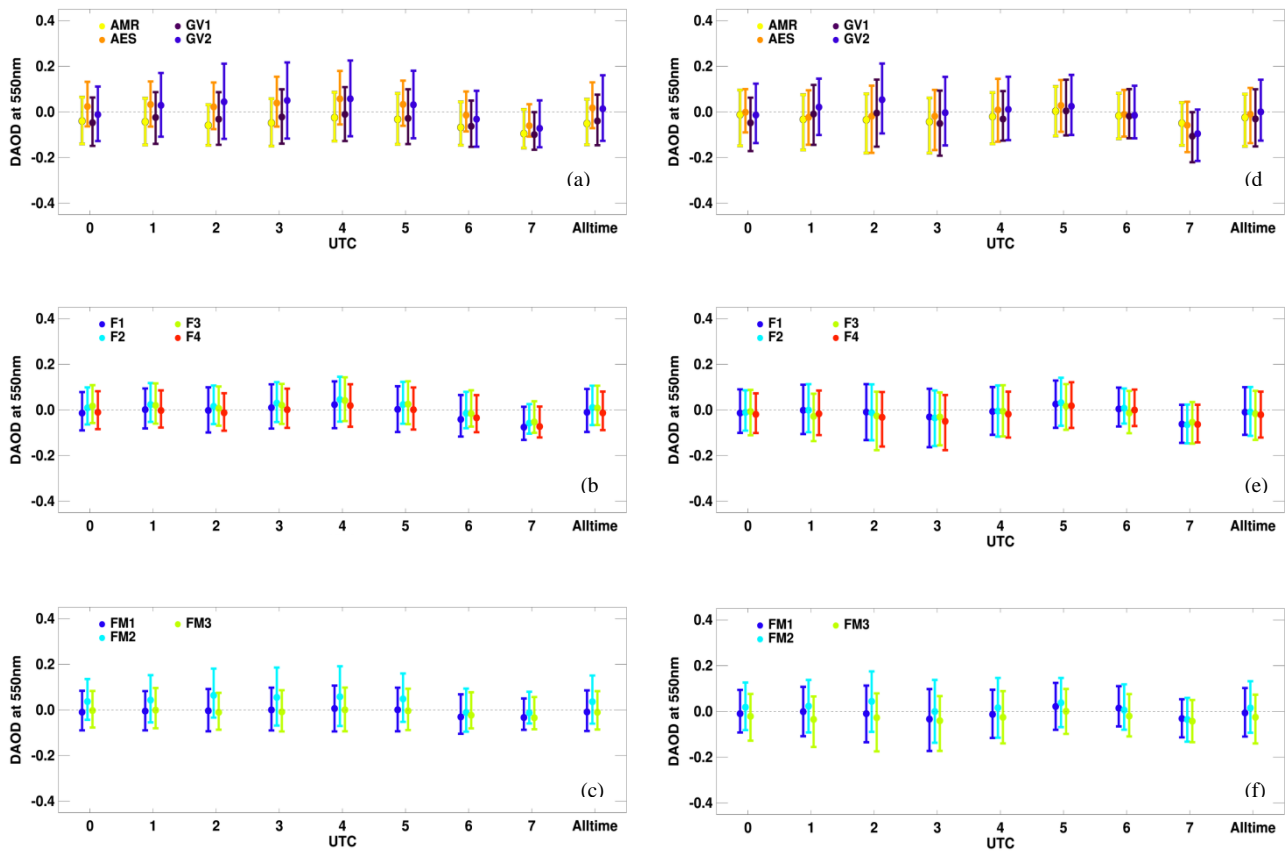


Figure 8. Same as Figure 7, but for the observation time in UTC.

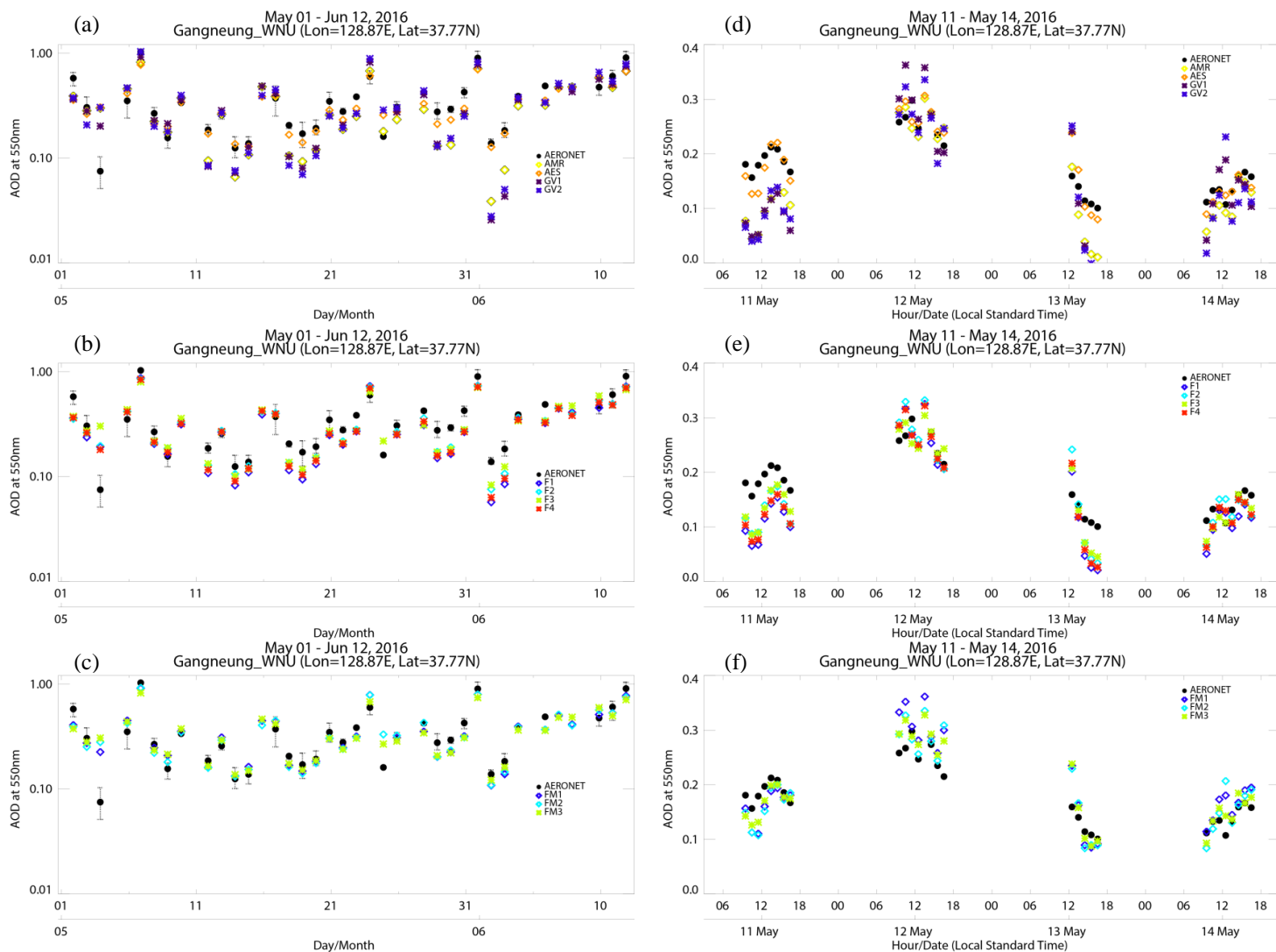


Figure 9. Time series of the daily average AODs at Gangneung WNU site during the KORUS-AQ campaign from (a) respective satellite, (b) ensemble-mean, and (c) MLE fusion. The black-filled circle represents AERONET AOD, and the error bar represents 1-SD of daily AERONET AODs. The diurnal variation in AODs from 11 to 14 May 2016 is shown in the right column, where (d) is the respective satellite, (e) is fused, and (f) is MLE products.

Table 4. Accuracy evaluation of outside of GOCI area of AMR, AES, F3, and FM3 AODs.

| Without GOCI domain | KORUS- AQ AMR | KORUS- AQ AES | KORUS- AQ F3 | KORUS- AQ FM3 | EMeRGe AMR | EMeRGe AES | EMeRGe F3 | EMeRGe FM3 |
|---------------------------|---------------------|---------------------|--------------------|---------------------|---------------|---------------|--------------|---------------|
| N | 1959 | 1958 | 1958 | 1958 | 2610 | 2610 | 2610 | 2610 |
| R | 0.699 | 0.658 | 0.713 | 0.707 | 0.794 | 0.826 | 0.829 | 0.821 |
| RMSE | 0.238 | 0.305 | 0.225 | 0.223 | 0.278 | 0.233 | 0.269 | 0.279 |
| MBE | -0.098 | 0.130 | 0.041 | 0.015 | -0.135 | -0.055 | -0.145 | -0.158 |
| GCOS | 25.6 | 25.6 | 27.3 | 26.5 | 26.8 | 34.1 | 29.0 | 27.5 |